

RESEARCH ARTICLE

10.1002/2016JA023727

GPS detection of ionospheric Rayleigh wave and its source following the 2012 Haida Gwaii earthquake

Key Points:

- Ionospheric Rayleigh waves are detected by GPS and agree well with BPR measurements
- A strong correlation is found between ionospheric Rayleigh waves and vertical ground motions
- The vertical ground motion is the dominated source of ionospheric Rayleigh waves

Correspondence to:

S. Jin,
sgjin@shao.ac.cn;
sgjin@yahoo.com

Citation:

Jin, S., R. Jin, and D. Li (2017), GPS detection of ionospheric Rayleigh wave and its source following the 2012 Haida Gwaii earthquake, *J. Geophys. Res. Space Physics*, 122, 1360–1372, doi:10.1002/2016JA023727.

Received 23 NOV 2016

Accepted 12 JAN 2017

Accepted article online 14 JAN 2017

Published online 30 JAN 2017

Shuanggen Jin¹ , Rui Jin¹, and D. Li^{2,3}

¹Shanghai Astronomical Observatory, Chinese Academy of Sciences, Shanghai, China, ²School of Communication and Information Engineering, Shanghai University, Shanghai, China, ³Department of Geomatics Engineering, Bulent Ecevit University, Zonguldak, Turkey

Abstract The processes and sources of seismo-ionospheric disturbances are still not clear. In this paper, coseismic ionospheric disturbances (CIDs) are investigated by dual-frequency GPS observations following the $M_w=7.8$ earthquake as results of the oblique-thrust fault in the Haida Gwaii region, Canada, on 28 October 2012. Results show that the CIDs with an amplitude of up to 0.15 total electron content units (TECU) are found with spreading out at 2.20 km/s, which agree well with the Rayleigh wave propagation speed at 2.22 km/s detected by the bottom pressure records at about 10 min after the onset. The CIDs are a result of the upward propagation acoustic waves triggered by the Rayleigh wave in sequence from near field to far field. The strong correlation is found between the CIDs and the vertical ground motion recorded by seismometers nearby the epicenter. The total electron content (TEC) series from lower-elevation angle GPS observations have higher perturbation amplitudes. Furthermore, the simulated ionospheric disturbance following a vertical Gauss pulse on the ground based on the finite difference time domain method confirms the ionospheric Rayleigh wave signature in the near field and the vertical ground motion dependence theoretically. The vertical ground motion is the dominant source of the ionospheric Rayleigh wave and affects the CID waveform directly.

1. Introduction

Studies on seismo-ionospheric disturbances can provide insights on solid-Earth and ionospheric coupling and ionospheric anomaly behaviors. Early studies on ionospheric responses to earthquakes began in the 1960s [Davies and Baker, 1965; Leonard and Barnes, 1965]. Seismic ionospheric effects were extracted from ionosondes near the epicenter of the 1964 Alaskan earthquake for the first time. However, due to the limited continuity of the observations, it was hard to get a profound and comprehensive understanding of the seismic ionospheric disturbance morphologies and coupling processes between the ground motion and ionospheric dynamics. Until 1990s, GPS has become a powerful tool not only for monitoring Earth's ground deformation [Jin and Park, 2006] but also for sounding the Earth's space environment [Jin et al., 2012; Afraimovich et al., 2013; Jin et al., 2014]. Since the first time seismic ionospheric anomalies were observed by GPS total electron content (TEC) after the 1994 Northridge earthquake in California, USA [Calais and Minster, 1995], a number of studies have been performed to study preseismic/coseismic ionospheric disturbances related to earthquakes and tsunamis [Afraimovich et al., 2001; Liu et al., 2010; Astafyeva et al., 2013; Rolland et al., 2013; Occhipinti et al., 2013]. It is proved that the existence of acoustic traveling ionospheric disturbance originated in the epicenter [Jin et al., 2015]. Nowadays, the increasing number of continuously operating GPS stations provides us abundant observations to monitor the detailed pattern and evolution of ionospheric perturbations following earthquakes [Afraimovich et al., 2010; Ducic et al., 2003; Rolland et al., 2011; Jin et al., 2014]. Recently, the detailed seismic ionospheric disturbances for the 2011 Tohoku earthquake ($M_w=9.0$) related to the seismic Rayleigh waves (2–3 km/s), acoustic waves (0.3–1.5 km/s), and gravity waves (0.1–0.3 km/s) were investigated and revealed by over 1000 Global Navigation Satellite Systems (GNSS) observations from the GPS Earth Observation Network in Japan [Rolland et al., 2011; Occhipinti et al., 2013]. The dense TEC disturbances clearly showed acoustic-gravity waves generated at the epicenter, acoustic waves coupled with Rayleigh wave, as well as gravity waves coupled with the propagation of the following tsunami [Occhipinti et al., 2013]. Furthermore, the frequency of detrended TEC perturbations showed the largest power spectral density (PSD) of 1.3–1.8 mHz. Higher-frequency signals with 3.83 and 5.83 mHz in TEC variations existed only near the epicenter region, which may be due to the attenuation with the disturbance propagation [Jin et al., 2014].

Ground motion at millimeters per second could induce neutral atmospheric disturbances at hundreds of meters per second at ionospheric height [Ducic *et al.*, 2003; Jin *et al.*, 2015]. On the one hand, the Earth's atmosphere is a natural "low-pass" filter with a few millihertz of high-frequency attenuation, while the attenuation of low-frequency signal during its upward propagation is rather small [de Groot-Hedlin *et al.*, 2011]. The acoustic-gravity waves at several millihertz following earthquakes are detectable at ionospheric height due to the atmospheric amplification and low attenuation for low-frequency disturbance. The previous researches indicated that the ionospheric perturbations could be detected in three categories: acoustic wave above the focal region, gravity wave, and secondary ionospheric perturbation induced by the Rayleigh wave that is a seismic surface wave causing the ground to shake in an elliptical motion [Ducic *et al.*, 2003; Heki *et al.*, 2006; Jin *et al.*, 2014, 2015]. With the decrease of neutral atmospheric mass density from the ground to the ionospheric height, the atmosphere amplifies the disturbance during its upward propagation exponentially [Artru *et al.*, 2004]. However, with the divergence of the epicenter surroundings and source types (such as wind, epicenter terrain, and focal mechanism), it remains challenging to get a full picture of seismic ionospheric disturbances and to know the ionospheric disturbance mechanism [Astafyeva *et al.*, 2014; Cahyadi and Heki, 2015; Reddy and Seemala, 2015], although the appearance and pattern of coseismic ionospheric disturbances (CIDs) following earthquakes were detected under certain conditions [Astafyeva *et al.*, 2011, 2013]. For example, Astafyeva *et al.* [2013] detected the multisegment structure of the seismic fault of the 2011 Tohoku-oki earthquake from high-rate ionospheric GPS data.

However, the mechanism coupling the solid Earth to the atmosphere and ionosphere is still not clear. Normally, the vertical displacement in the earthquake zone plays a more important role in the formation of seismic ionospheric disturbance [e.g., Astafyeva and Heki, 2009; Jin *et al.*, 2015], while the relationship between the earthquake displacement and the ionospheric variation is not understood comprehensively up to now. Furthermore, the relationship between seismic ionospheric disturbances and ground motion is still debated [e.g., Ducic *et al.*, 2003; Rolland *et al.*, 2011; Maruyama *et al.*, 2012]. In this paper, the coseismic ionospheric disturbances (CIDs) following the 2012 $M_w=7.8$ Haida Gwaii earthquake are extracted from the near-field dense GPS observations. The CID propagation features and directional divergences are analyzed and discussed as well as the correlation and coupling between the ionospheric disturbance and ground vertical movement.

2. Observations and Methods

The $M_w=7.8$ earthquake occurred in Haida Gwaii region, Canada (52.61°N, 132.06°W) at 03:04:24 UT on 28 October 2012 as recorded in the Global Centroid Moment Tensor (CMT) catalog. GPS observations from hundreds of stations are available near the epicenter from the University NAVSTAR Consortium (UNAVCO) data center. In this study, we aim to investigate the near-field seismic ionospheric disturbances using data within 2000 km near the epicenter. Figure 1 shows the ionospheric pierce points (IPPs) distribution in the top left panel, epicenter, and GPS stations. A good TEC coverage from GPS dual-frequency observation is available around the $M_w=7.8$ Haida Gwaii earthquake, especially in the southeast of the epicenter. In addition, the ground motion data in the near field are also used from IRIS (Incorporated Research Institutions for Seismology, <http://www.iris.edu>) seismic stations and DART (Deep-Ocean Assessment and Reporting of Tsunamis) bottom pressure records (BPRs) nearby (Figure 1) [National Oceanic and Atmospheric Administration, 2005]. These continuous multiobservations of ground motion and ionospheric variations with high precision and resolution (especially for temporal resolution) provide us a good opportunity to study the seismic ionospheric response to the 2012 $M_w=7.8$ Haida Gwaii earthquake.

The equations of carrier phase (L) and code observations (pseudorange P) of dual-frequency GPS are expressed as [Jin *et al.*, 2008, 2016]

$$\begin{aligned} L_{k,j}^i &= \lambda_k \phi_{k,j}^i = \rho_{0,j}^i - d_{\text{ion},k,j}^i + d_{\text{trop},j}^i + c(\tau^i - \tau_j) - \lambda_k (b_{k,j}^i + N_{k,j}^i) \\ P_{k,j}^i &= \rho_{0,j}^i + d_{\text{ion},k,j}^i + d_{\text{trop},j}^i + c(\tau^i - \tau_j) + d_{q,k}^i + d_{q,k,j}^i + \varepsilon_j^i \end{aligned} \quad (1)$$

where subscript k stands for the frequency ($k=1, 2$), superscripts i and j represent the satellite and ground-based GPS receiver, respectively, ρ_0 is the true distance between the GPS receiver and satellite, d_{ion} and d_{trop} are the ionospheric and tropospheric delays, c is the speed of light in vacuum space, τ is the satellite or receiver clock offset, b is the phase delay of satellite and receiver instrument bias, d_q is the code delay of satellite

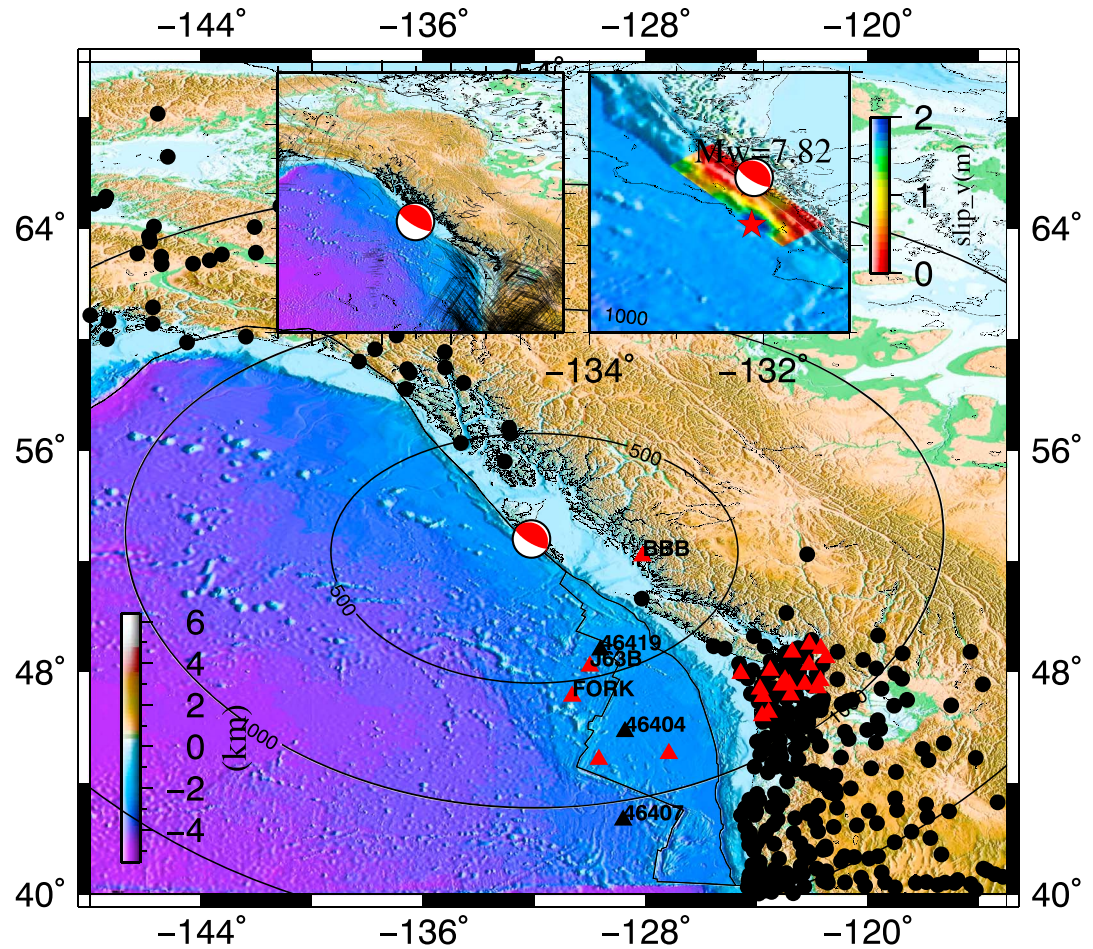


Figure 1. The distribution of GPS stations, seismic stations, and BPRs near the Haida Gwaii earthquake epicenter. The black dots show the location of GPS stations; the red and black triangles show the location of seismic stations and BPRs, respectively. The focal mechanism is provided by the Global Centroid Moment Tensor (CMT) project ([http://www-globalcmt.org](http://www.globalcmt.org)). The top left subfigure presents the IPP distribution during 03:00–04:00 UT. The top right subfigure presents the vertical slips in the focal region, which were calculated using the slip model of the 2012 $M_w = 7.8$ Haida Gwaii earthquake [Lay et al., 2013]. The background topography data used here are the ETOP1 model provided by NOAA.

and receiver instrument bias, λ is the carrier wavelength, ϕ is the total carrier phase between the satellite and receiver, N is the ambiguity of the carrier phase, and ε is other residuals. Ignoring the high-order ionospheric effect in the Appleton-Hartree equation, the ionospheric total electron content (TEC) along the signal path could be derived from the dual-frequency GPS carrier phase and pseudorange measurements as [Jin et al., 2008, 2012]

$$\begin{aligned} \text{TEC} &= \frac{f_1^2 f_2^2}{40.28(f_1^2 - f_2^2)} (L_1 - L_2 + \lambda_1(N_1 + b_1) - \lambda_2(N_2 + b_2)) \\ &= \frac{f_1^2 f_2^2}{40.28(f_2^2 - f_1^2)} (P_1 - P_2 - (d_1 - d_2)) \end{aligned} \quad (2)$$

where L and P are the carrier phase and pseudorange observations (meter), f is the carrier frequency, λ and N are the carrier phase wavelength and integer ambiguity, d and b are the instrument biases, and the subscripts stand for the frequency number. Here carrier phase measurements are used to study the seismic ionospheric disturbances with the high precision. A simple cosine mapping function is used to convert slant TEC to vertical TEC for the disturbance propagation analysis. A zero-phase Butterworth filter is used to remove the background variation in the TEC series as its flat frequency response in the pass band. A fourth order is selected for

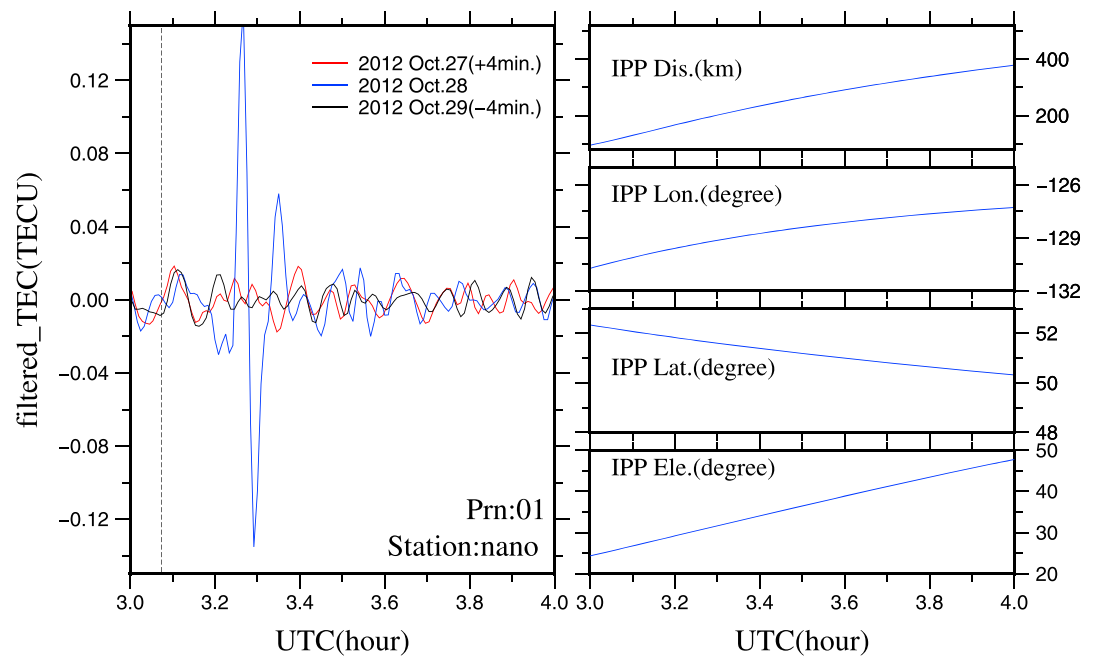


Figure 2. Filtered TEC variations during 03:00–04:00 UT on 27–29 October detected by GPS observations at station NANO from satellite G01 (i.e., PRN01). The $M_w=7.8$ Haida Gwaii earthquake onset is marked by a vertical dashed line. The right panel shows the epicentral distances, longitudes, latitudes, and satellite elevations for corresponding ionospheric pierce points, respectively.

the filter that has been proved to be effective for seismic ionospheric disturbance extraction from TEC series [Calais *et al.*, 1998]. In this study, we focus on the relationship between Rayleigh wave seismo-ionospheric disturbance and ground motion. So the passband is selected as 2 mHz (near the acoustic cutoff frequency around a 150 km altitude) to 8 mHz (half of Nyquist frequency for GPS observations with 30 s sampling rate). The selected GPS stations provide observations with 15 or 30 s intervals. Here we choose 8 mHz as the upper cutoff frequency to avoid distortion signals caused by the filtering.

3. Results and Discussion

3.1. Ionospheric Disturbances From GPS

Significant ionospheric disturbances in TEC are found from dense GPS observations following the 2012 Haida Gwaii earthquake. For example, Figure 2 shows the filtered TEC series derived from station NANO’s PRN01 observations on the onset, previous, and next days. The TEC series in the previous and next days are delayed and advanced 4 min for the same IPP (ionospheric pierce point) location in the Earth-centered Earth-fixed coordinate system. The TEC temporal variations in 4 min are relatively small as compared to the TEC horizontal gradient caused by IPP motion at the low satellite elevation angle. Pronounced ionospheric disturbances with an amplitude of up to 0.15 TECU units (TECU, 1 TECU = $10^{16} \text{ el m}^{-2}$) appear following the onset, while the filtered TEC variations in the previous and next days are within 0.02 TECU dominated by the GPS measurement noise. After reaching the peak around 03:15 UT, the disturbance amplitude decreases with the time and the distance far from the epicenter. No geomagnetic or solar events are recorded during this period as well as other sources that could trigger ionospheric disturbances in this region. Therefore, the large ionospheric disturbances above the earthquake’s epicenter region are most related to the earthquake. As shown by the filtered TEC from three consecutive days in similar positions, the zero-phase fourth-order Butterworth filter with 2–8 mHz catches well the seismo-ionospheric disturbances by removing the local TEC background variation.

Figure 3 shows the distribution of the detrended TEC disturbances at each IPP within 1500 km far from the epicenter during 03:09–03:21 UT. The filtered TEC amplitudes are shown from -0.05 to 0.05 TECU. TEC disturbances beyond the range of the color bar are represented, with the highest value shown for a better view of

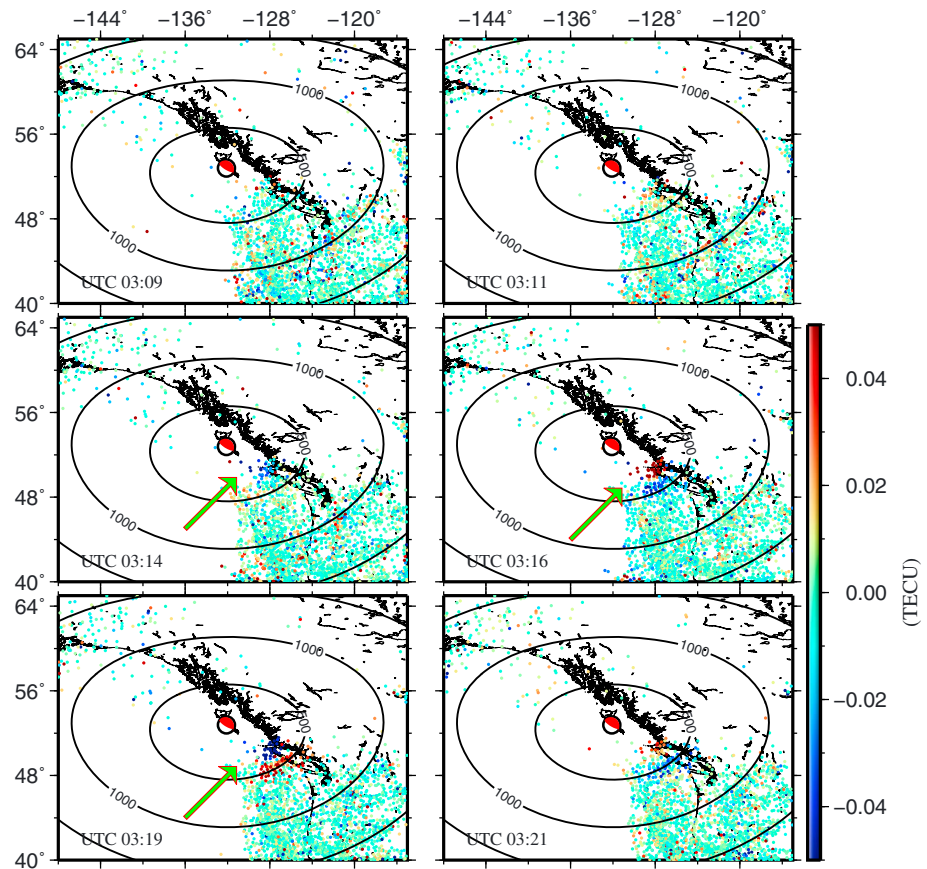


Figure 3. TEC perturbations within 1500 km far from the epicenter following the Haida Gwaii earthquake detected by GPS data during 03:09–03:21 UT. The green arrows show pronounced wavelike disturbances in the southeast in the snaps of 03:14 UT, 03:16 UT, and 03:19 UT.

the wavelike perturbation. Actually, the amplitude could be higher than 0.1 TECU in the focal regions as shown in Figure 1. Pronounced wavelike disturbances appear in the southeast in the snaps of 03:14 UT, 03:16 UT, and 03:19 UT. The disturbances are first observed near the epicenter and spread out to several hundred kilometers away. TEC disturbance turns positive peak to negative (or negative to positive) in 3 min for the same region as shown in the snaps 03:16 UT and 03:19 UT. Until 03:21 UT, almost no TEC disturbance is detected. Compared to the southeast (SE), almost no disturbances are observed in the northwest. Due to the limitation of IPP distribution, the TEC variation in the northeast and southwest is not available.

The most pronounced ionospheric disturbances are detected by GPS observations from the PRN01 since the corresponding IPP locations in 1 h following the onset is the closest to the epicenter. Figure 4 shows the PRN01 traveling time diagram of CIDs propagating in the SE following the earthquake with the distance and the time. The zero in horizontal and vertical axes corresponds to the onset and the epicenter location of the 2012 $M_w = 7.8$ Haida Gwaii earthquake. The slope line is determined by the corresponding locations and epochs of separated disturbance peaks. Here the “delay” and “velocity” correspond to the first appearance epoch and group propagation velocity of seismic disturbances following the Haida Gwaii earthquake at 2–8 mHz. The CID propagation speed and appearance epoch are determined by the linear fitting for the locations and epochs at the maximum amplitudes. The results show that the seismic ionospheric disturbance first appears 10.77 min after the onset and propagates at a speed of 2.20 km/s. Although earthquake-induced tsunamis with a maximum height of 7.6 m sheltered from storm waves and 13 m at the inlet were reported [Leonard and Bednarski, 2014], it could not propagate to the ionospheric height from the sea surface in 10 min, while the propagation speed of the tsunami-generated gravity wave is much smaller than the one presented here for regions with less than 2000 m of water depth ($v_{\text{tsunami}} = \sqrt{gh}$, g is the acceleration of

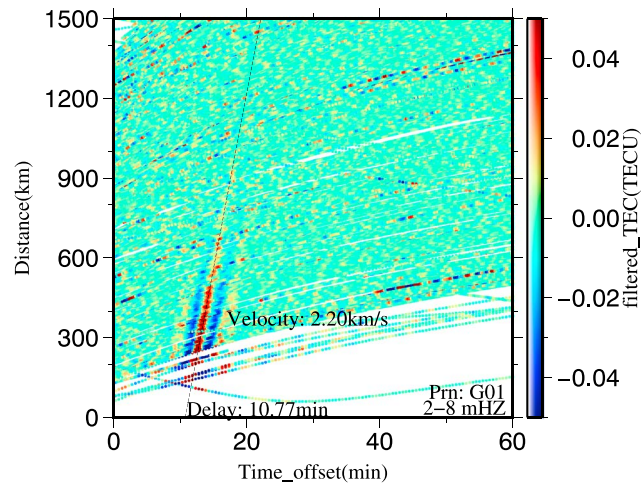


Figure 4. Travel time diagram of CIDs detected by GPS observations of PRN01. The zero in horizontal and vertical axes corresponds to the onset and the epicenter location of the $M_w = 7.8$ Haida Gwaii earthquake in 2012. The slope line is determined by the corresponding locations and epochs of separated disturbance peaks. Here the “delay” and “velocity” correspond to the first appearance epoch and group propagation velocity of seismic disturbances following the Haida Gwaii earthquake at 2–8 mHz.

gravity and h is the water depth) [Occhipinti *et al.*, 2008, 2013]. Furthermore, the CIDs should be dominated by the acoustic mode as a result of 2–8 mHz filtering, while the tsunami-related ionospheric disturbance is with a central frequency of 1–2 mHz at gravity wave modes [Jin *et al.*, 2014; Occhipinti *et al.*, 2013]. Grawe and Makela [2015] reported tsunami-generated CIDs following the $M_w = 7.8$ earthquake, while it appeared in the far field with more than 3000 km away during 08:30–09:00 UT. The coseismic horizontal acoustic wave above the focal region is another possible source of seismo-ionospheric disturbance. It is induced by the refraction of upward atmospheric pulse due to the vertical neutral density gradient. However, the sound speed at the ionospheric height is around 1 km/s. Therefore, the detected CIDs are mostly related to the Rayleigh wave that propagates with a much higher speed. Note that the locations of CID, seismometers, and DART BPRs are shown in Figures 1 and 3, and the 2.20 km/s propagating seismic ionospheric disturbance is just above the region where the Rayleigh wave group velocity is about 2.22 km/s. However, other superposition of acoustic and Rayleigh waves may affect CIDs and make the apparent velocity between the acoustic and Rayleigh waves [e.g., Astafyeva *et al.*, 2013], which needs to be further investigated with available data in the future.

3.2. CID Amplitudes and Effects

It is well known that the intersection between GPS signal paths and Earth’s ionospheric electron concentrated region varies with the satellite motion. The GPS observation geometry has an effect on amplitudes of the observed CIDs [Afraimovich *et al.*, 1992]. As the omnidirectional GPS observations are not available around the epicenter, we mainly discussed the effect of satellite elevation angle on the observed CID amplitudes. Figure 5 presents the ionospheric disturbance peaks of the TEC series obtained from PRN01 and PRN11 observations during 03:08–03:20 UT when the pronounced seismic ionospheric disturbance appeared. Here we only present the result of PRN01 and PRN11 since the corresponding IPPs are mainly distributed in the region with the most pronounced CIDs. Obvious amplitude attenuation with the epicentral distance is shown in both the observations of PRN01 and PRN11. Due to the station distribution and satellite position, satellite elevation angles are similar with each other for separated satellite observations. It is a good opportunity to see the CID distance delay without the satellite elevation angle effect. A third-order polynomial fitting is applied to fit the relationship between epicentral distances and disturbance amplitudes as shown in the top left panel of Figure 5. The result of higher-order polynomial fitting is similar with the one from the third-order fitting, implying that the CID amplitudes attenuate cubically with the epicentral distance approximately in the near field. As the epicentral distance increases, the ionospheric temporal-spatial dynamic background diverges more, which could lead to different attenuated patterns. It is expected that the quasi-cubical attenuate is not the case in the far field. Comparing to PRN01, the disturbance observed by PRN11

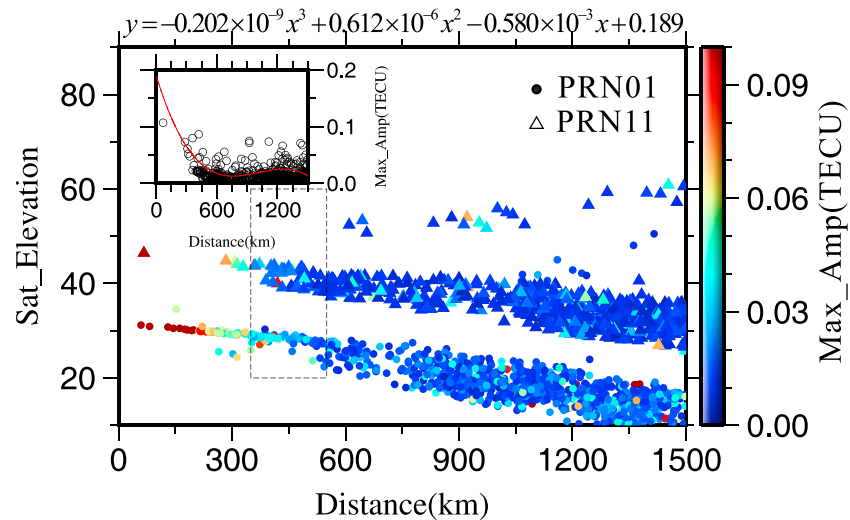


Figure 5. Maximum ionospheric disturbance amplitudes of filtered TEC series obtained from PRN01 and PRN11 observations during the 03:08–03:20 UT. The colored circle is the peak amplitudes for TEC series from PRN01 observations, and the triangle is the peak amplitudes for TEC series from PRN11. The third-order polynomial fitting between epicentral distances and disturbance amplitudes is shown in the top left panel.

observation is much weaker, especially in 350–550 km as marked by the dashed rectangle in Figure 5. Although the IPPs have similar locations, the observed disturbance amplitudes are higher for observations with lower satellite elevation angles. It is consistent with the statistical features of the Rayleigh wave-related seismo-ionospheric disturbance amplitudes from six GPS TEC series following different earthquakes proposed by Rolland *et al.* [2011].

However, the cosine mapping function from slant TEC to vertical TEC may have some effects. GPS TEC observations are not sensible to the acoustic perturbation propagating in parallel with the signal path direction, as GPS ionospheric measurements are integrated along the line of sight between GPS satellites and receivers. The GPS TEC disturbance effect from the local ionospheric electron density increase or decrease induced by the wavelike disturbance would be attenuated when it propagates along the signal path. For regions within 200 km, the elevation angle effect is not obvious. The maximum disturbance amplitude is similar for 30–50° elevation angles. It indicates that ionospheric disturbances induced by the oblique acoustic wave existed in the focal region. The Rayleigh wave-induced ionospheric disturbance is not a unique dominant seismo-ionospheric effect. In addition, interaction between the movements of charged particles in Rayleigh waves and magnetic fields might selectively attenuate the seismic ionospheric disturbances [Afraimovich *et al.*, 2001; Heki and Ping, 2005; Rolland *et al.*, 2013].

3.3. Ground Vertical Motion From Seismic and DART Data

In order to confirm the CID's Rayleigh wave dependence, postseismic vertical ground motion in the near field is investigated. Using the same band-pass filtering, the normalized vertical ground motions from the observations of 23 broadband high-gain seismometers and three DART BPRs within 1500 km epicentral distance are presented in Figure 5. The station locations are marked in Figure 1. Not like the high sampling rate seismic data, the BPR series released by DART normally have a 15 min interval for the tidal report at the quiet state, while the sampling rate is up to 1 min or 15 s when a sea bottom pressure disturbance is detected [Meinig *et al.*, 2005]. Here the sampling rate of the released DART BPRs during 03:00–04:00 UT is 1 min, so we interpolated the BPRs at the quiet time to a 1 min interval with the spline interpolation unifying the data interval and avoiding the filtering alias. Considering the Rayleigh wave propagation anisotropy related to the crust structure diversity, we present the vertical displacement disturbance of solid ground surface and seafloor separately in the left and right panels of Figure 6. The Rayleigh waves with similar waveform in 2–8 mHz are detected by both seismic and DART BPR data. The southwestern Rayleigh wave group velocity is determined with the wave crest appearance epochs and locations. The ground surface Rayleigh waves show a

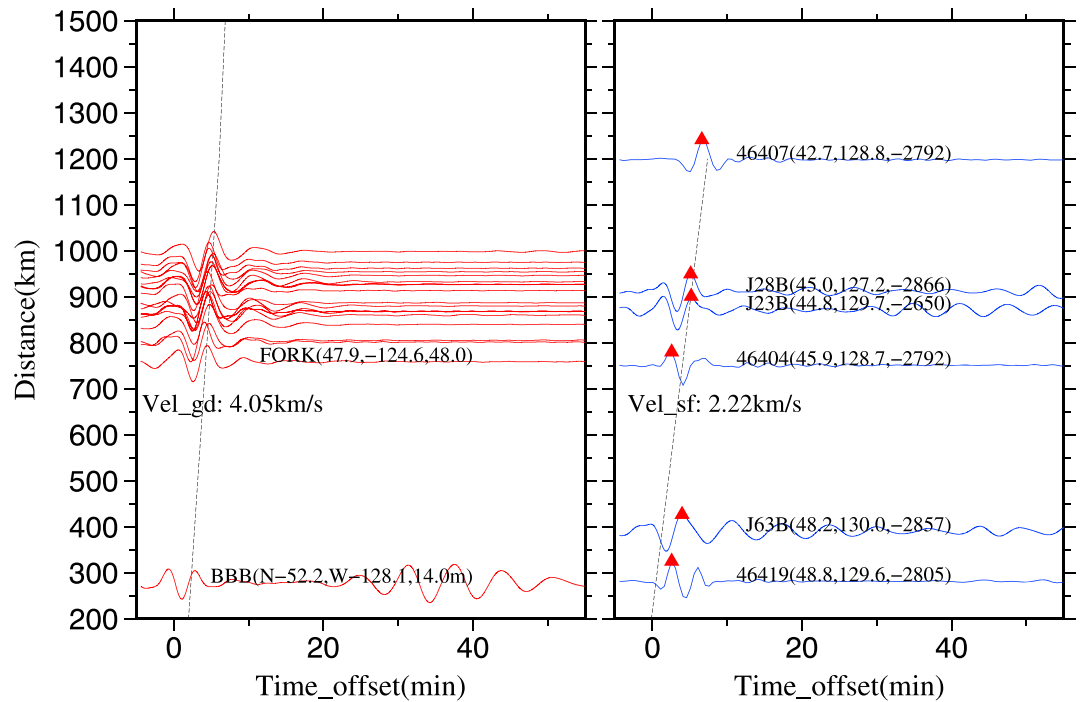


Figure 6. Vertical ground motion in 2–8 MHz detected by the vertical broadband high-gain seismometers and DART BPRs (46419, 46404, and 46407) near the epicenter. The locations of selected stations are shown in Figure 1. The vertical displacements at solid ground surface and seafloor are presented separately on the left and right panels. The series are normalized to the corresponding maximum disturbance amplitudes. The zero line for each series is adjusted to the station epicentral distance (in the vertical axis). The locations and elevations of DART BPRs and selected seismometers are marked. The unmarked stations are mainly distributed near the Seattle coast with 0–300 m elevation.

high propagation velocity of up to about 4.05 km/s, while the one on the seafloor is about 2.22 km/s which agrees well with the CIDs' propagation speed detected by GPS data, indicating that the observed CIDs are induced by the Rayleigh wave in the seafloor. Note that the island station FORK is also located in the CID regions while the corresponding Rayleigh signature in the vertical displacement series appears earlier in a faster mode. The observed CID in the southeast is more closely related to the Rayleigh wave propagation in the seafloor.

It should be pointed out that the Rayleigh wave appearance epoch is almost at the onset according to the linear fitting estimation from the vertical ground displacement records on the seafloor. The results are based on the point source and constant propagation disturbance. While the real fault dip slip is far away from the point source as shown in Figure 1, the constant propagation should not be the real case within the scale of the focal region. Here we focus on the most pronounced CIDs 300–700 km away from the epicenter. Since not enough GPS observations are available to see the ionospheric disturbances over the Seattle region, we could not validate the existence of the ionospheric Rayleigh signature with a speed of 4.05 km/s for corresponding region following this earthquake. The Rayleigh wave-induced CID at such a speed is possible [Maruyama *et al.*, 2012]. It is believed that the anisotropy of the Rayleigh wave could be an important source of CID propagation divergence in different directions.

3.4. Correlation Between Ground Motion and CIDs

Although directional divergence of the Rayleigh wave has a significant effect on its propagation velocity, the waveform is similar within 1000 km far from the epicenter as discussed above. The vertical ground displacement series should agree with each other after time delay adjustment. The superposed series are used to reduce the subtle disturbance resulting from other factors, such as measurement noise and local environment effect. The DART station 46419, which is just located below the CID, is set as the reference series for the determination of time delay between different series using the cross-correlation technique. The same

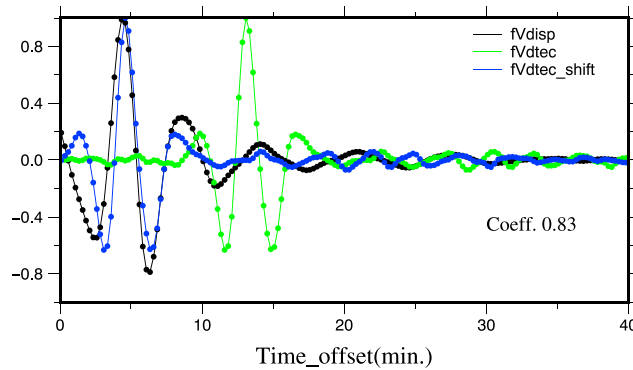


Figure 7. Correlation between the superposed TEC and ground vertical displacements in the southwest of the epicenter. The black line is the normalized superposed vertical displacement series, the green line is the normalized superposed filtered TEC series, and the blue line is a copy of the green one but 8.8 min in advance. Here the vertical displacement series is opposite to the records, namely, negative value meaning the upward motion, for intuitive illustration of the correlation.

The 2–8 mHz ionospheric CIDs observed by GPS data show high consistency with the vertical ground motion. The correlation coefficient is up to the maximum, i.e., 0.83 with an 8.8 min delay, and the small difference with the linear fitting results could be induced by the noise in the TEC series.

The simplified acoustic ray tracing for a horizontally stratified atmosphere [Garcés *et al.*, 1998] is applied to get a view of the wavefront and trajectories of upward propagation disturbances. As shown in Figure 8, the upward acoustic perturbation propagates to around 150 km altitudes after 8.8 minutes, where the electron density is high enough to induce a detectable TEC disturbance for GPS observations. It is up to the ionospheric F_2 peak height after about 14 min, which is consistent with the observed TEC peak epoch as shown in Figure 7. Note that the propagation direction of oblique acoustic waves is deflected dramatically as it goes through atmospheric layers with large mass density gradient and trapped around the 200 km altitude. Then it could trigger the traveling ionospheric disturbance at the sound speed. So, it should not be the dominant source of seismo-ionospheric effect detected by GPS data in the southeast of the epicenter. We know that the vertical coupling at the interface between the atmosphere and Earth surface is much more efficient than

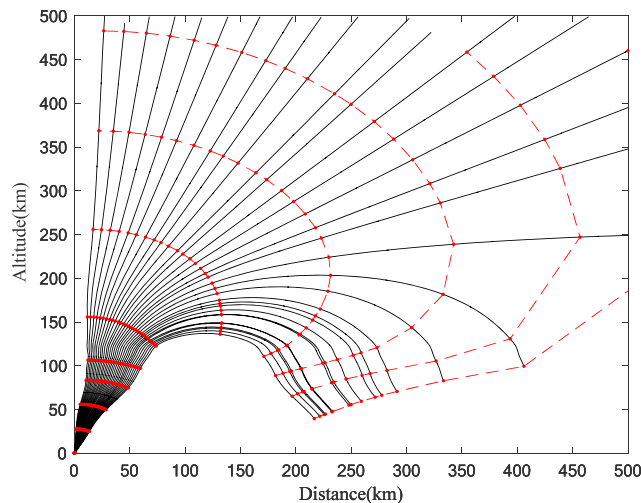


Figure 8. Acoustic ray tracing for zenith 60–90° from a point perturbation source. Here the sound and wind velocity profiles for the focal region on 28 October 03:15 UT are derived from NRLMSISE-00 atmospheric model and HWM07 [Drob *et al.*, 2008]. The red line is the equal-time contours with 2 min interval.

processing is used to get the superposed TEC series. The TEC with the highest sum of the correlation coefficients is selected as the reference series [Kiryushkin and Afraimovich, 2007]. It is expected that the distortion of observed waveforms could be induced by the satellite movement [Garrison *et al.*, 2007]. Fortunately, the radial movement is small when compared to the CID scale as shown in Figures 3 and 4 in 10 min. For the quasi-radial propagation disturbance, we ignored the satellite motion effect. Both superposed displacement and TEC series are normalized to corresponding maximum values as shown in Figure 7.

the horizontal one. Usually, the initial disturbance at the bottom of the atmosphere from ground motion is an upward pulse except for the epicenter region where an oblique acoustic disturbance is possible as large-amplitude slips induced by an oblique fault rupture [Astafyeva *et al.*, 2011]. The high correlation coefficient between the 2–8 mHz ground vertical displacements and seismo-ionospheric disturbance indicates that the Rayleigh ionospheric disturbance is the result of vertical ground motion at the solid Earth-atmosphere coupling frequencies in corresponding regions. Therefore, it has the potential of ionospheric disturbance detection using ground motion observations.

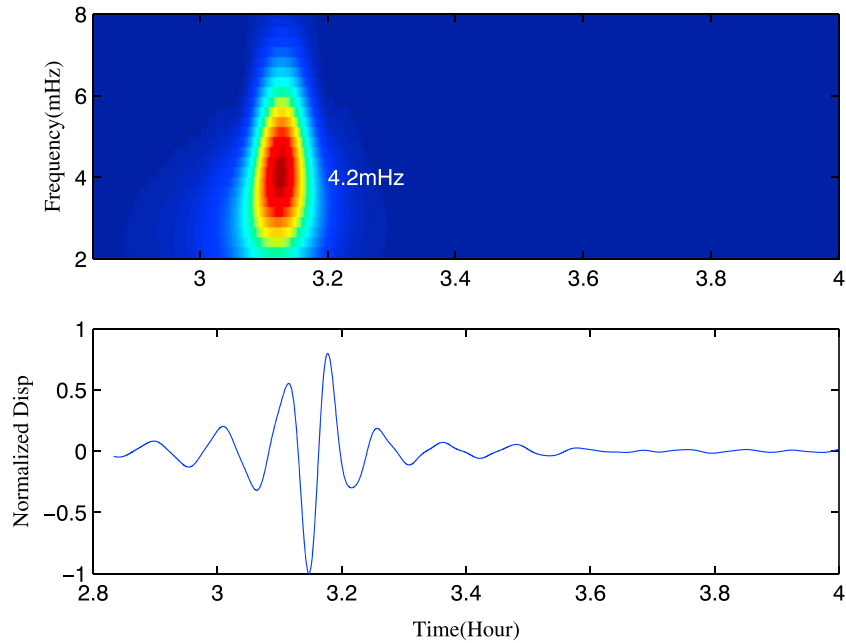


Figure 9. Frequency spectrum (upper) and normalized displacements (bottom) of the 2012 $M_w=7.8$ Haida Gwaii earthquake.

4. Coupling of the Rayleigh Wave and Ground Motions

The neutral disturbance triggered by the ground displacement could be simulated with the state equation, momentum, and mass conservation [de Groot-Hedlin, 2007; Rolland et al., 2011]. Utilizing the electron continuity and momentum equation [Shinagawa et al., 2007], the electron disturbance could be simulated. In our simulation, wind effects, viscosity, and heat conduction are not considered, which does not make great sense for the 2–8 mHz acoustic wave propagation from the ground to ionospheric height. A finite difference time domain method is applied to get the neutral perturbation induced by the Rayleigh wave in the two-dimensional stratified atmosphere centered at the epicenter [de Groot-Hedlin et al., 2011]. The NRLMSISE-00 model is used to get the vertical profiles of neutral particle density and sound velocity [Picone et al., 2002]. The wind velocity profiles are derived from the HWM07 [Drob et al., 2008]. The perturbation source is simulated using the product of cosine and sine functions as follows:

$$v_{\text{disp},z=0}(x, t) = A \text{sinc} \left[2\pi f_b \left((t - t_0) - \frac{|x|}{v_{\text{Reigh}}} \right) \right] \cos \left[2\pi f_c \left((t - t_0) - \frac{|x|}{v_{\text{Reigh}}} \right) \right] \quad (3)$$

where x is the epicentral distance, A is vertical ground speed at the earthquake onset time t_0 , f_b is the perturbation frequency bandwidth, f_c is the perturbation central frequency, and v_{Reigh} is the Rayleigh wave propagation speed (2.2 km/s). The background ionospheric electron density was from IRI-2012 [Bilitza et al., 2014]. Figure 9 is the simulated frequency spectrum (upper) and normalized displacements (bottom) of the 2012 $M_w=7.8$ Haida Gwaii earthquake, which shows that the power spectrum peak is 4.2 mHz, namely, the perturbation central frequency.

Assuming that the perturbations are small, electron density disturbance is derived by integrating the continuity equation. Here the neutral electron density collision frequency is computed based on the empirical formula [Kelley, 2009]

$$v_e = 5.4 \times 10^{-10} n_n T_e^{0.5} + \left[34 + 4.18 \ln \left(\frac{T_e^3}{n_e} \right) \right] n_e T_e^{-1.5} \quad (4)$$

where v_e is the speed of electron disturbance and n_e , n_n , and T_e are the electron density, neutral atmospheric molecular density, and electron temperature, respectively. The perturbation of the electron density can be

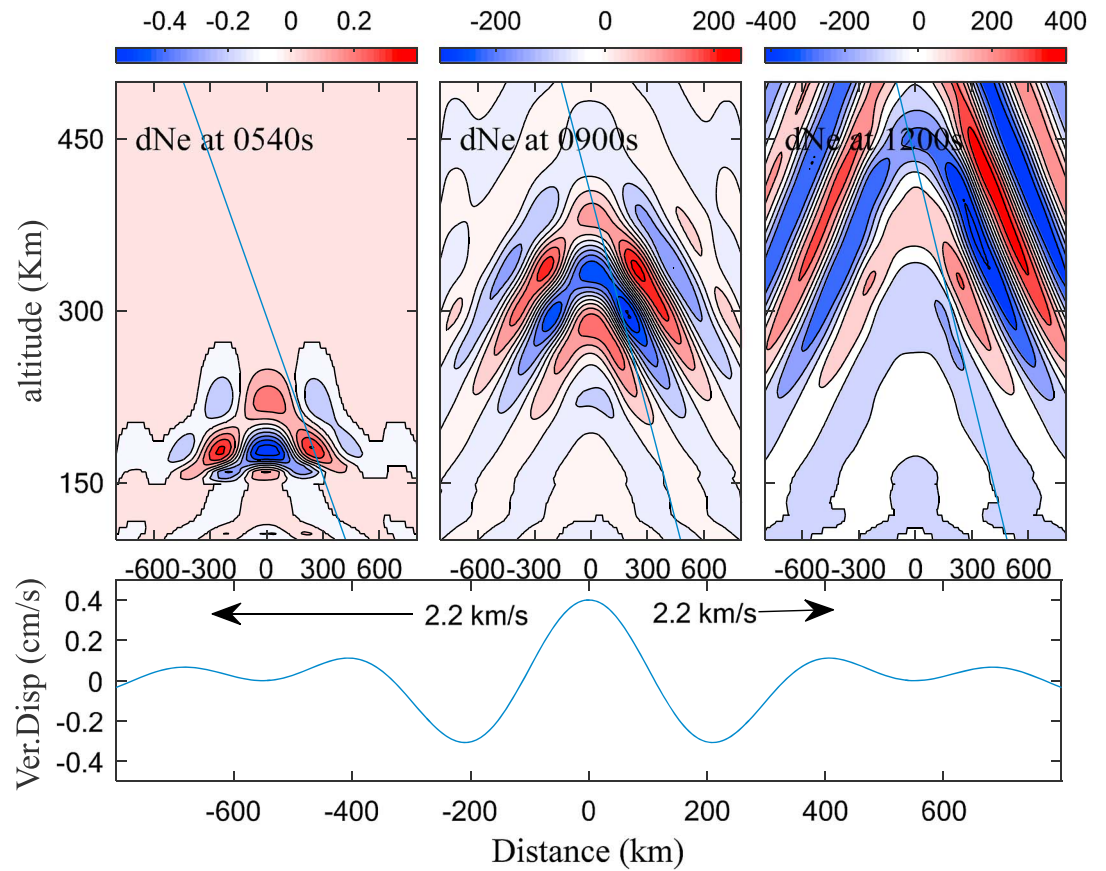


Figure 10. The electron density disturbances (10^{10} electron/m³) following the moving vertical ground motion source as shown in the bottom. The blue lines in the contour plots are the signal path for station NANO PRN01.

obtained by integrating the continuity equation for the charge density from the explosion time t_0 to the observation time t [Dautermann et al., 2009]:

$$\delta N(\vec{r}, t) = -\frac{\partial N}{\partial z} \int_{t_0}^t v_{e,z}(\vec{r}, t) dt - N(z) \int_{t_0}^t \nabla \cdot v_{e,z}(\vec{r}, t) dt \quad (5)$$

where δN is the disturbance of the electron number density (N).

Figure 10 shows the simulated ionospheric electron density disturbances at 9 to 20 min after the onset in the NE-SW direction (epicentral azimuth = 135°). Consistent with the time delay from observations and acoustic ray tracing mentioned above, the pronounced ionospheric disturbance appears about 9 minutes at around 150 km altitudes. The perturbation enhances with its upward propagation amplified by the decreasing neutral particle density and increasing electron density. As an example, the signal path between station NANO and satellite PRN01 is marked by the blue lines in Figure 10 (the satellite elevation angle varies 25–34°). It is obvious to see that the ground motion-induced ionospheric wavelike disturbances can be observed through the signal path across the positive and negative disturbance regions in sequence. With the ideal GPS observation geometry (i.e., the single path is quasi-parallel to the disturbance wavefront), the observed wave disturbance should be near the real case. Then the high correlation between the vertical ground motion and the disturbance at ionospheric height is expected. The geomagnetic field effect on the seismic ionospheric disturbance, i.e., the higher disturbance amplitude in the southwest direction, is shown especially after the disturbance arrived at the F_2 layer height, while the weak effect probably cannot explain the absence of seismic ionospheric effect in the northeast, which may be a strong attenuation of the Rayleigh wave-coupled waves due to the combination effect of the seismic source, the geomagnetic field, and the observation geometry [Rolland et al., 2011]. A lack of efficient GPS observations for seismic ionospheric

effect detection is the major reason. Apparently, the disturbance signal would be attenuated if the GPS signal path is near the perpendicular direction of the wavefront as shown in Figure 10.

4. Conclusion

In this paper, the seismo-ionospheric disturbances following the 2012 $M_w = 7.8$ earthquake are investigated and studied using GPS data near the epicenter. Results show that the seismo-ionospheric disturbances at a speed of about 2 km/s are mainly related to the Rayleigh wave signature in the ionospheric height. The seismic ionospheric effect is a result of the upward propagation acoustic wave induced by the Rayleigh wave rather than the direct effect of the focal rupture. With the “ideal” GPS observation geometry, higher observed CID amplitudes are found for the observations with lower satellite elevation angles, i.e., the signal path near the direction of the disturbance wavefront. This is also evidence that the observed CIDs are the result of the upward acoustic wave rather than the horizontal acoustic wave that could induce ionospheric disturbance traveling with the sound speed. CID propagation agrees well with the group velocity of the Rayleigh wave in corresponding regions. Rayleigh wave isotropy should be an important source for the divergence of CID propagation. After removing the noise by superposition, the strong correlation between the vertical ground motion and CID variation is found. The vertical ground motion should be the dominant source of the CIDs and affects the CID waveform directly. Our simulation results further confirm the features of electron density perturbation following this earthquake. A high correlation could be expected in the GPS TEC series if the signal path is nearly parallel to the disturbance wavefront.

Acknowledgments

Great appreciation is extended to UNAVCO for providing the GPS data, IRIS (Incorporated Research Institutions for Seismology, <http://www.iris.edu>) seismic data, and DART (Deep-Ocean Assessment and Reporting of Tsunamis, <http://www.ngdc.noaa.gov>) bottom pressure records (BPRs) as well as X. Liu for discussion. This work was supported by the National Natural Science Foundation of China (NSFC) Project (grant 11573052).

References

- Afraimovich, E. L., A. I. Terekhov, M. Y. Udodov, and S. V. Fridman (1992), Refraction distortions of transionospheric radio signals caused by changes in a regular ionosphere and by travelling ionospheric disturbances, *J. Atmos. Terr. Phys.*, *54*(7–8), 1013–1020, doi:10.1016/0021-9169(92)90068-V.
- Afraimovich, E. L., N. P. Perevalova, A. V. Plotnikov, and A. M. Uralov (2001), The shock-acoustic waves generated by the earthquakes, *Ann. Geophys.*, *19*(4), 395–409, doi:10.5194/angeo-19-395-2001.
- Afraimovich, E. L., F. Ding, V. Kiryushkin, E. Astafeyeva, S. G. Jin, and V. Sankov (2010), TEC response to the 2008 Wenchuan earthquake in comparison with other strong earthquakes, *Int. J. Remote Sens.*, *31*(13), 3601–3613, doi:10.1080/01431161003727747.
- Afraimovich, E. L., et al. (2013), A review of GPS/GLONASS studies of the ionospheric response to natural and anthropogenic processes and phenomena, *J. Space Weather Space Clim.*, *3*, A27, doi:10.1051/swsc/2013049.
- Artru, J., T. Farges, and P. Lognonne (2004), Acoustic waves generated from seismic surface waves: Propagation properties determined from Doppler sounding observations and normal-mode modeling, *Geophys. J. Int.*, *158*(3), 1067–1077, doi:10.1111/j.1365-246X.2004.02377.x.
- Astafeyeva, E., and K. Heki (2009), Dependence of waveform of near-field coseismic ionospheric disturbances on focal mechanisms, *Earth Planet Space*, *61*, 939–943, doi:10.1186/BF03353206.
- Astafeyeva, E., L. Rolland, P. Lognonne, K. Khelifi, and T. Yahagi (2013), Parameters of seismic source as deduced from 1 Hz ionospheric GPS data: Case-study of the 2011 Tohoku-oki event, *J. Geophys. Res. Space Physics*, *118*, 5942–5950, doi:10.1002/jgra50556.
- Astafeyeva, E., L. Rolland, and A. Sladen (2014), Strike-slip earthquakes can also be detected in the ionosphere, *Earth Planet. Sci. Lett.*, *405*, 180–193, doi:10.1016/j.epsl.2014.08.024.
- Astafeyeva, E. I., P. Lognonne, and L. Rolland (2011), First ionospheric images of the seismic fault slip on the example of the Tohoku-oki earthquake, *Geophys. Res. Lett.*, *38*, L22104, doi:10.1029/2011GL049623.
- Bilitza, D., D. Altadil, Y. Zhang, C. Mertens, V. Truhlik, P. Richards, L.-A. Mckinnell, and B. Reinisch (2014), The International Reference Ionosphere 2012—a model of international collaboration, *J. Space Weather Space Clim.*, *4*, A07, doi:10.1051/swsc/2014004.
- Cahyadi, M. N., and K. Heki (2015), Coseismic ionospheric disturbance of the large strike-slip earthquakes in North Sumatra in 2012: M_w dependence of the disturbance amplitudes, *Geophys. J. Int.*, *200*, 116–129, doi:10.1093/gji/ggu343.
- Calais, E., and J. Minster (1995), GPS detection of ionospheric perturbations following the January 17, 1994, Northridge earthquake, *Geophys. Res. Lett.*, *22*(9), 1045–1048, doi:10.1029/95GL00168.
- Calais, E., J. Minster, M. Hofton, and M. Hedlin (1998), Ionospheric signature of surface mine blasts from Global Positioning System measurements, *Geophys. J. Int.*, *132*(1), 191–202, doi:10.1046/j.1365-246x.1998.00438.x.
- Dautermann, T., E. Calais, P. Lognonne, and G. S. Mattioli (2009), Lithosphere—atmosphere—ionosphere coupling after the 2003 explosive eruption of the Soufriere Hills Volcano, Montserrat, *Geophys. J. Int.*, *179*(3), 1537–1546, doi:10.1111/j.1365-246X.2009.04390.x.
- Davies, K., and D. M. Baker (1965), Ionospheric effects observed around the time of the Alaskan earthquake of March 28, 1964, *J. Geophys. Res.*, *70*, 2251–2253, doi:10.1029/JZ070i009p02251.
- de Groot-Hedlin, C. D. (2007), Finite difference modeling of infrasound propagation to local and regional distances, in *Proceedings of the 29th Monitoring Research Review*, Denver, Colo., 25–27 September 2007, pp. 836–844, Rep. LA-UR-07-5613, Natl. Nucl. Security Admin., Washington, D. C.
- de Groot-Hedlin, C. D., M. Hedlin, and K. Walker (2011), Finite difference synthesis of infrasound propagation through a windy, viscous atmosphere: Application to a bolide explosion detected by seismic networks, *Geophys. J. Int.*, *185*(1), 305–320, doi:10.1111/j.1365-246X.2010.04925.x.
- Drob, D. P., et al. (2008), An empirical model of the Earth’s horizontal wind fields: HWM07, *J. Geophys. Res.*, *113*, A12304, doi:10.1029/2008JA013668.
- Ducic, V., J. Artru, and P. Lognonne (2003), Ionospheric remote sensing of the Denali earthquake Rayleigh surface waves, *Geophys. Res. Lett.*, *30*(18), 223–250, doi:10.1029/2003GL017812.
- Garcés, M. A., R. Hansen, and K. Lindquist (1998), Travel times for infrasonic waves propagating in a stratified atmosphere, *Geophys. J. Int.*, *135*(1), 255–263, doi:10.1046/j.1365-246X.1998.00618.x.

- Garrison, J. L., S. Lee, J. Haase, and E. Calais (2007), A method for detecting ionospheric disturbances and estimating their propagation speed and direction using a large GPS network, *Radio Sci.*, *42*, RS6011, doi:10.1029/2007RS003657.
- Grawe, M. A., and J. J. Makela (2015), The ionospheric responses to the 2011 Tohoku, 2012 Haida Gwaii, and 2010 Chile tsunamis: Effects of tsunami orientation and observation geometry, *Earth Space Sci.*, *2*, 472–483, doi:10.1002/2015EA000132.
- Heki, K., and J. Ping (2005), Directivity and apparent velocity of the co-seismic ionospheric disturbances observed with a dense GPS array, *Earth Planet. Sci. Lett.*, *236*, 845–855, doi:10.1016/j.epsl.2005.06.010.
- Heki, K., Y. Otsuka, N. Choosakul, N. Hemmakorn, T. Komolmis, and T. Maruyama (2006), Detection of ruptures of Andaman fault segments in the 2004 great Sumatra earthquake with coseismic ionospheric disturbances, *J. Geophys. Res.*, *111*, B09313, doi:10.1029/2005JB004202.
- Jin, R., S. G. Jin, and G. Feng (2012), M_DCB: Matlab code for estimating GNSS satellite and receiver differential code biases, *GPS Solutions*, *16*(4), 541–548, doi:10.1007/s10291-012-0279-3.
- Jin, S., R. Jin, and J. H. Li (2014), Pattern and evolution of seismo-ionospheric disturbances following the 2011 Tohoku earthquakes from GPS observations, *J. Geophys. Res. Space Physics*, *119*, 7914–7927, doi:10.1002/2014JA019825.
- Jin, S. G., and P. Park (2006), Strain accumulation in South Korea inferred from GPS measurements, *Earth Planets Space*, *58*(5), 529–534, doi:10.1186/BF03351950.
- Jin, S. G., O. Luo, and P. Park (2008), GPS observations of the ionospheric F_2 -layer behavior during the 20th November 2003 geomagnetic storm over South Korea, *J. Geod.*, *82*(12), 883–892, doi:10.1007/s00190-008-0217-x.
- Jin, S. G., G. Occhipinti, and R. Jin (2015), GNSS ionospheric seismology: Recent observation evidences and characteristics, *Earth Sci. Rev.*, *147*, 54–64, doi:10.1016/j.earscirev.2015.05.003.
- Jin, S. G., R. Jin, and D. Li (2016), Assessment of BeiDou differential code bias variations from multi-GNSS network observations, *Ann. Geophys.*, *34*(2), 259–269, doi:10.5194/angeo-34-259-2016.
- Kelley, M. C. (2009), *The Earth's Ionosphere: Plasma Physics and Electrodynamics*, 2nd ed., Acad. Press (Elsevier), San Diego, Calif.
- Kiryushkin, V. V., and E. L. Aframovich (2007), Determining the parameters of ionospheric perturbation caused by earthquakes using the quasi-optimum algorithm of spatiotemporal processing of TEC measurements, *Earth Planets Space*, *59*(4), 267–278, doi:10.1186/BF03353104.
- Lay, T., L. Ye, H. Kanamori, et al. (2013), The October 28, 2012 M_w 7.8 Haida Gwaii under thrusting earthquake and tsunami: Slip partitioning along the queen charlotte fault transpressional plate boundary, *Earth Planet. Sci. Lett.*, *375*(8), 57–70, doi:10.1016/j.epsl.2013.05.005.
- Leonard, L. J., and J. M. Bednarski (2014), Field survey following the 28 October 2012 Haida Gwaii tsunami, *Pure Appl. Geophys.*, *171*(12), 3467–3482, doi:10.1007/s00024-014-0792-0.
- Leonard, R. S., and R. A. Barnes (1965), Observation of ionospheric disturbances following the Alaska earthquake, *J. Geophys. Res.*, *70*(5), 1250–1253, doi:10.1029/JZ070i005p01250.
- Liu, J. Y., H. Tsai, C. Lin, M. Kamogawa, Y. I. Chen, C. H. Lin, B. S. Huang, S. B. Yu, and Y. H. Yeh (2010), Co-seismic ionospheric disturbances triggered by the Chi-Chi earthquake, *J. Geophys. Res.*, *115*, A08303, doi:10.1029/2009JA014943.
- Maruyama, T., T. Tsugawa, H. Kato, M. Ishii, and M. Nishioka (2012), Rayleigh wave signature in ionograms induced by strong earthquakes, *J. Geophys. Res.*, *117*, A08306, doi:10.1029/2012JA017952.
- Meinig, C., S. E. Stalin, A. I. Nakamura, and H. B. Milburn (2005), Real-time deep-ocean tsunami measuring Monitoring, and Reporting System: The NOAA DART II Description and Disclosure Rep., NOAA, Pacific Marine Environmental Laboratory.
- National Oceanic and Atmospheric Administration (2005), Deep-Ocean Assessment and Reporting of Tsunamis (DART(R)), National Geophysical Data Center, NOAA, doi:10.7289/V5F18WNS.
- Occhipinti, G., E. Kherani, and P. Lognonne (2008), Geomagnetic dependence of ionospheric disturbances induced by tsunamigenic internal gravity waves, *Geophys. J. Int.*, *173*(3), 753–765, doi:10.1111/j.1365-246X.2008.03760.x.
- Occhipinti, G., L. Rolland, P. Lognonne, and S. Watada (2013), From Sumatra 2004 to Tohoku-oki 2011: The systematic GPS detection of the ionospheric signature induced by tsunamigenic earthquakes, *J. Geophys. Res. Space Physics*, *118*, 3626–3636, doi:10.1002/jgra.50322.
- Picone, J. M., A. E. Hedin, D. P. Drob, and A. C. Aikin (2002), NRLMISE-00 empirical model of the atmosphere: Statistical comparisons and scientific issues, *J. Geophys. Res.*, *107*(A12), 1468, doi:10.1029/2002JA009430.
- Reddy, C. D., and G. K. Seemala (2015), Two-mode ionospheric response and Rayleigh wave group velocity distribution reckoned from GPS measurement following M_w 7.8 Nepal earthquake on 25 April 2015, *J. Geophys. Res. Space Physics*, *120*, 7049–7059, doi:10.1002/2015JA021502.
- Rolland, L. M., P. Lognonne, and H. Munekane (2011), Detection and modeling of Rayleigh wave induced patterns in the ionosphere, *J. Geophys. Res.*, *116*, A05320, doi:10.1029/2010JA016060.
- Rolland, L. M., M. Vergnolle, J.-M. Nocquet, A. Sladen, J.-X. Dessa, F. Tavakoli, H. R. Nankali, and F. Cappa (2013), Discriminating the tectonic and non-tectonic contributions in the ionospheric signature of the 2011, M_w 7.1, dip-slip Van earthquake, Eastern Turkey, *Geophys. Res. Lett.*, *40*, 2518–2522, doi:10.1002/grl.50544.
- Shinagawa, H., T. Iyemori, S. Saito, and T. Maruyama (2007), A numerical simulation of ionospheric and atmospheric variations associated with the Sumatra earthquake on December 26, 2004, *Earth Planets Space*, *59*(9), 1015–1026, doi:10.1186/BF03352042.